Research Article Vol. 64, No. 11 / 10 April 2025 / Applied Optics 2949

applied optics

Angle-robust hyperspectral imaging based on quasi-random metal metasurfaces and cross-correlation optimization

Nan Chen, Xin Zhou, Luxi Yin, Rui Chen, and Jianwen Dong*

School of Physics and State Key Laboratory of Optoelectronic Materials and Technologies, Sun Yat-sen University, Guangzhou, 510275, China
**dongjwen@mail.sysu.edu.cn*

Received 18 February 2025; revised 10 March 2025; accepted 14 March 2025; posted 17 March 2025; published 4 April 2025

Snapshot hyperspectral imaging based on metasurface optical filters combined with computational spectral reconstruction offers extensive applicability for miniature and compact spectral systems. However, existing designs are constrained by the angular dispersion response of metasurfaces and the limited cross-correlation among transmission spectra, leading to imperfect reconstruction and application challenges. In this paper, we propose a method for angle-robust hyperspectral imaging based on quasi-random metal metasurfaces that enables a 40° field-of-view within the 500–700 nm wavelength range. Furthermore, we introduce a cross-correlation optimization technique based on an orthogonal matrix to align with the principle of compressed sensing theory, achieving a cross-correlation of 0.49 with an average angle sensitivity of 1.11%. The results show angle-robust hyperspectral reconstruction with an average spectral fidelity of 91.64% for computational spectrometers, along with excellent performance for hyperspectral imaging. This advancement enhances the accuracy of hyperspectral reconstruction for large field-of-view spectral devices and close-up analysis, demonstrating substantial potential for integration into portable spectral devices.

https://doi.org/10.1364/AO.559959

1. INTRODUCTION

Spectral imaging technology has evolved from monochromatic to trichromatic (RGB), multispectral, and hyperspectral imaging, leading to enhanced spectral resolution. Hyperspectral technology, known for its high-resolution capabilities, has expanded from its initial use in remote sensing to diverse applications in precision agriculture, food safety, environmental monitoring, and biomedical engineering, largely driven by progress in device miniaturization [1]. Despite these advancements, the design and manufacture of these systems often result in large volumes and intricate structures that pose challenges for integration [2,3]. Moreover, the traditional step-by-step scanning methods for acquiring spectral or spatial information significantly prolong acquisition time and increase operational complexity and maintenance costs [4].

Snapshot spectral imaging using micro-nano filter arrays as spectral elements offers an effective solution to this problem. Related schemes include nanowires [5,6], quantum dot arrays [7], photonic crystal arrays [8], and metasurface arrays [9–12]. Among these, metasurfaces, a two-dimensional planar structure with subwavelength sizes, stand out for their ability to capture and scatter incident light, enabling flexible manipulation over electromagnetic waves' amplitude, frequency, phase, and polarization [13–15]. They serve as an advantageous alternative to traditional spectral elements, providing effective information modulation for spectral reconstruction within a compressed sensing framework. This method requires fewer units than spectral channels, facilitating miniaturization, integration, and compatibility with complementary metal oxide semiconductor (CMOS) technologies [16–19].

However, the angle issue is a significant concern in spectral reconstruction [20,21]. While most commercial spectral camera lenses typically have an angle of 30°, this value can be significantly reduced to 2° when using metasurfaces for computational reconstruction. Metasurfaces display a pronounced angular dispersion response, which makes their transmission spectra highly dependent on the incident angle. In the subsequent spectral reconstruction, the measurement matrix composed of these transmission spectra varies with the incident angle, thereby impacting the reconstructed effect and spectral fidelity. It is common practice to mitigate angular interference by employing collimation devices [21] or conducting prior calibration [22], but additional components or corresponding calibration devices inevitably lead to complex systems or operations. A more effective approach to address this issue is to develop angle-insensitive spectral elements using metal metasurfaces [23]. However, these metal metasurfaces with simple modes are challenging to generate diverse transmission responses and result in high

cross-correlation, making it difficult to satisfy the requirement of compressed sensing theory [24,25], which in practice hinders the accurate reconstruction of spectral information and requests more optical metasurfaces for information capture.

In this paper, we propose an angle-robust hyperspectral imaging design based on quasi-random metal metasurfaces (QRMM). The design achieves an average angle sensitivity of 0.77% under a 40° field-of-view within the wavelength range of 500–700 nm. Additionally, we introduce a cross-correlation optimization technique based on an orthogonal matrix to satisfy the requirement of compressed sensing theory and effectively reduce the cross-correlation by 0.41. Meanwhile, the average angle sensitivity slightly increases to 1.11%. We verify the performance in the context of computational spectrometers and hyperspectral imaging, using a compressed-sensing-based computational spectral reconstruction algorithm. The results demonstrate angle-robust hyperspectral reconstruction with an average spectral fidelity of 91.64% for computational spectrometers and an average spectral image fidelity of 89.98% for hyperspectral imaging. These results at a 40° field-of-view achieve comparable fidelity to the normal incidence performance in the existing study [24]. More significantly, when evaluated using the fidelity metric based on inner products, our method demonstrates superior performance compared to the existing study at a 30° field-of-view, which requires more metasurfaces [23]. This confirms the effectiveness of capturing hyperspectral information under oblique incidence and highlights the significant advancement of our approach.

2. METASURFACE DESIGN

A. Structure of Quasi-random Metal Metasurfaces

To overcome design space limitations and achieve high angular robustness in spectral devices, we propose a design of etching gold (Au) metasurface supercells following a predefined rule. Figure 1(a) depicts the configuration of a series of 50 nm thick Au nanopillars arranged on a silicon dioxide (SiO_2) substrate with a square periodic distribution. The aforementioned metasurface supercells are combined into a 5 × 5 QRMM filter on a CMOS image sensor to create a compact snapshot spectrometer. Each supercell produces a unique spectral response, which is detected by the photodetector for spectral reconstruction. All simulations of transmission spectra are conducted using the finite-difference time-domain (FDTD) method, with the refractive indices of Au and SiO_2 taken from [26] and [27].

Each metasurface supercell is generated by randomly etching in a C4-symmetric form with a 1.32 μm period, ensuring polarization insensitivity at normal incidence. To enhance the design flexibility, the supercell is divided into $2n \times 2n$ subcells on average, where n is a positive integer. These square subcells are characterized by a total of $n(n+1)/2$ numbers, as illustrated in Fig. 1(b). In this instance, the value of n is set to 3, yielding six numbers with a side length of 220 nm. Subcells with the same number are either etched with Au nanopillars of equivalent size or left unetched. To the extent feasible, the diameters of the etched Au nanopillars are selected from m non-repeating parameters, where m is a positive integer, forming a configuration scheme of $m+1$ numbers within a subcell. Here, Au nanopillars with diameters of 80, 100, and 120 nm are selected to form

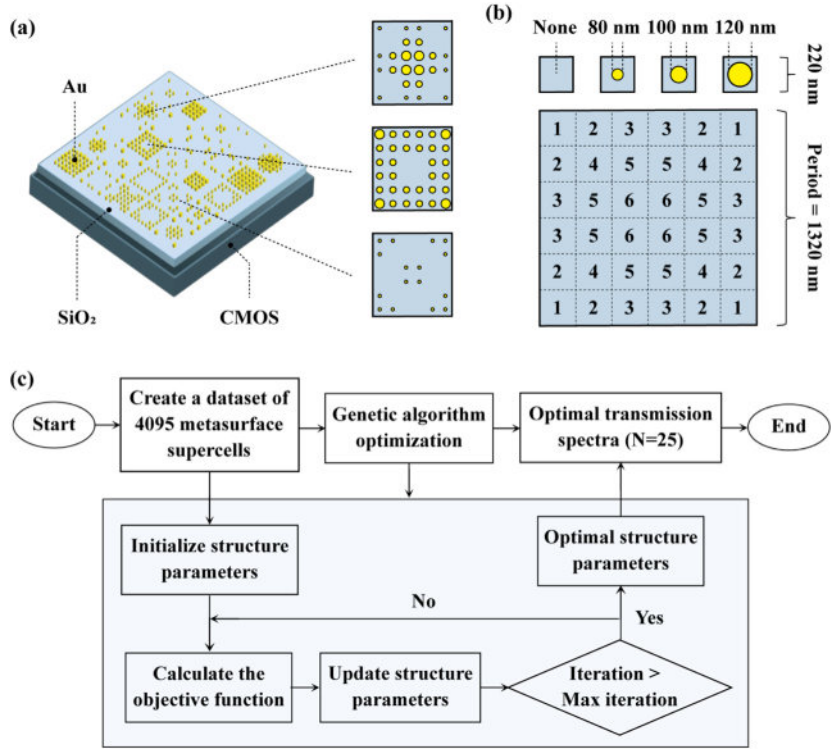

Fig. 1. (a) Schematic of a QRMM filter comprising 5 × 5 metasurface supercells integrated with a CMOS image sensor. (b) Schematic diagram of a metasurface supercell divided into 6 × 6 subcells. (c) Flowchart of genetic algorithm optimization for the QRMM filter, where the genetic algebra and population size are set as 500 and 25, respectively.

a four-number configuration scheme. This choice is guided by comprehensive experimental considerations, ensuring that the minimum diameter is achievable in manufacture and that the spacing between adjacent Au nanopillars exceeds 100 nm. It can thus be deduced that 4^6-1 configuration schemes are formed for a metasurface supercell, excluding the case where all subcells are unetched. In a more general quasi-random etching scenario, it can be concluded that $(m+1)^n-1$ metasurface supercells are obtained. This brings a substantial increase compared to only etched or unetched subcells, where only 2^n-1 metasurface supercells can be obtained. Consequently, the proposed QRMM filter design increases design freedom by leveraging the configuration possibilities of different subcells.

The geometric library comprising thousands of metasurface supercells is constructed using the described method, with the goal of selecting 25 metasurface supercells as a QRMM filter that exhibits low average angle sensitivity for spectral reconstruction. The optimal geometric parameters and configuration numbers are determined by a genetic algorithm, as illustrated in Fig. 1(c). The process begins with individual initialization, followed by screening based on the objective function to identify the most promising metasurface supercells for further optimization until the fitness function converges. The objective function is defined as follows:

$$\text{minimize}\left(\frac{1}{N}\sum_{i=1}^{N}\frac{||T_{i1}-T_{i2}||_1}{||T_{i1}||_1} - \alpha\cdot\frac{1}{N}\sum_{i=1}^{N}\sum_{j=1}^{N}\min_{i\neq j}||T_{i1}-T_{j1}||_2\right),\quad \alpha>0, \tag{1}$$

where $N=25$ is the number of metasurface supercells, α is the weight factor, T is the transmission spectra, and the subscripts 1 and 2 are the average polarization transmission spectra of normal incidence and oblique incidence. In this definition, T_{i1} and T_{j1} represent the transmission spectra of the ith and jth supercells under normal incidence, and T_{i2} represent the average polarization transmission spectra under oblique incidence. The first part in Eq. (1) represents the average angle sensitivity and is given by the following expression:

$$\sigma=\frac{1}{N}\sum_{i=1}^{N}\frac{||T_{i1}-T_{i2}||_1}{||T_{i1}||_1}, \tag{2}$$

which is defined as the average relative difference of transmission spectra under normal incidence and oblique incidence. In this study, an incident angle of 20° is chosen as the maximum oblique incidence angle to conduct the most stringent test, corresponding to a 40° field-of-view that exceeds the typical value for most camera lenses. Meanwhile, the minimum mutual differences among spectra expressed in the second part of Eq. (1) are maximized to facilitate the spectral reconstruction. The weight factor α, which represents the level of concern for angle sensitivity and minimum mutual differences, is chosen as 0.05.

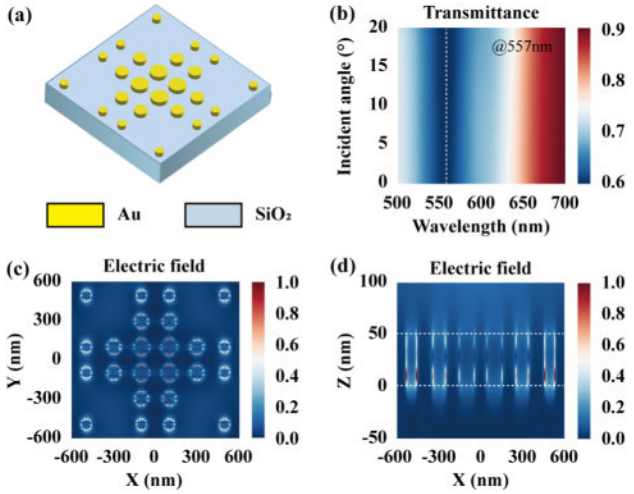

Fig. 2. (a) Metasurface supercell with three different sizes of Au nanopillars. (b) Transmission spectra for average polarization with the incident angle varying from 0° to 20°. The dashed line represents the resonance wavelength, corresponding to 557 nm. (c) Cross-sectional electric field distribution. (d) Longitudinal electric field distribution. The dashed lines represent the upper and lower surfaces of Au nanopillars with a height of 50 nm.

B. Principle of Quasi-random Metal Metasurfaces

To further confirm the angular robustness of the QRMM filter, we simulate the transmission spectra over various angles. Figure 2(a) shows a metasurface supercell with Au nanopillars in three different sizes, including 80, 100, and 120 nm. Figure 2(b) illustrates that the transmission spectra remain consistent when the incident angle varies from 0° to 20°. Additionally, we simulate the electric field profile of the metasurface supercell at the wavelength of 557 nm, including the cross-section and the longitudinal section, as shown in Figs. 2(c) and 2(d). The electric field propagates locally on the surface of the structure, indicating that the Au nanopillar arrays support localized surface plasmon resonance (LSPR) mode. This mode is activated by specific polarization and frequency, and the decoupling between adjacent subcells makes the metasurface supercell insensitive to the incident angle [28–31]. Consequently, the QRMM filter with high angular robustness can be obtained.

3. CROSS-CORRELATION OPTIMIZATION

A. Reconstruction and Optimization Principle

We optimize the geometric parameters and configuration numbers by genetic algorithm to achieve a QRMM filter with high angular robustness to construct the measurement matrix of the compressed sensing algorithm. The incident spectrum, $I(\lambda)$, is sampled and encoded by the QRMM filter to produce various transmission responses denoted by $T(\lambda)$, where λ is the incident wavelength. As shown in Fig. 3, the signal is recorded by a CMOS detector in a single snapshot mode and converted into electronic signals. And the signal intensity S recorded by the CMOS detector is given by the following expression:

$$S=\int_{\lambda_1}^{\lambda_M}T(\lambda)I(\lambda)\mathrm{d}\lambda, \tag{3}$$

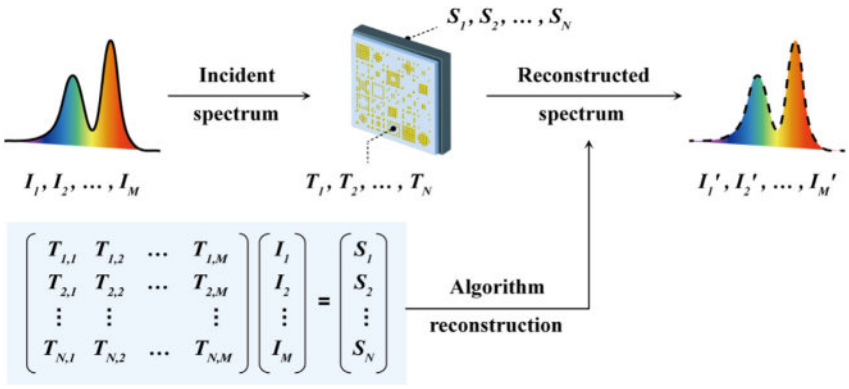

Fig. 3. Reconstruction principle of the compressed sensing algorithm.

where λ_1 and λ_M represent the lower and upper limits of the incident wavelength, respectively. Herein, $\lambda_1 = 500$ nm and $\lambda_M = 700$ nm. In practice, the incident spectrum $I(\lambda)$ is typically discretized into an M-dimensional vector to facilitate the solution. Similarly, the transmission spectra $T(\lambda)$ of the QRMM filter can be discretized into an $N \times M$ dimensional vector, and the signal S recorded on the CMOS sensor can be expressed as an N-dimensional vector for spectral reconstruction.

In the framework of compressed sensing, a low cross-correlation coefficient of the measurement matrix is essential to meet the requirement for spectral reconstruction [32,33]. However, metal metasurfaces, unlike dielectric ones with multiple resonance modes, tend to exhibit simple transmission responses and result in a high cross-correlation. To address this, we propose a cross-correlation optimization method using an orthogonal matrix to further process the QRMM filter. Here, N metasurface supercells are used for spectral reconstruction in Fig. 4(a), with the incident spectrum discretized into an M-dimensional vector. The orthogonal matrix then establishes relationships between the detected equivalent output signal S' and the equivalent filter T' as follows:

$$S' = T' I, \tag{4}$$

where the equivalent output signal S' and the equivalent filter T' can be expressed, respectively, by the orthogonal matrix as

$$S' = \theta S, \tag{5}$$

$$T' = \theta T, \tag{6}$$

where $S \in R^{N\times 1}$ is the original output signal, $T \in R^{N\times M}$ is the transmission spectra matrix, and $\theta \in R^{N\times N}$ is the orthogonal matrix. In accordance with the associative law of matrix multiplication, we can derive the following: $\theta(TI) = (\theta T)I$, indicating that multiplying the formula by an orthogonal matrix θ on the left serves equivalently to construct a new filter. In this context, the equivalent filter with reduced cross-correlation is acquired to satisfy the reconstruction requirement of compressed sensing.

An orthogonal matrix is composed of $N \times N$ discrete elements, each value ranging from $-K$ to K, where K represents a positive integer scaling factor. This factor ensures numerical

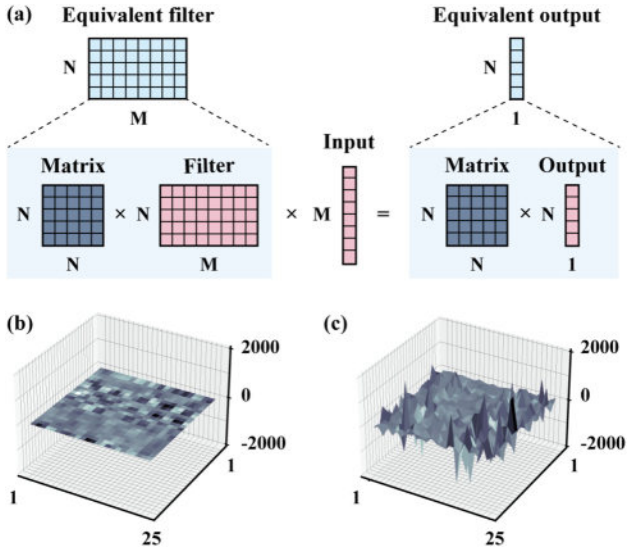

Fig. 4. (a) Schematic diagram of cross-correlation optimization based on an orthogonal matrix. (b) Orthogonal Matrix 1 with small absolute values. (c) Orthogonal Matrix 2 with large absolute values.

stability during optimization while enabling the construction of a parameterized matrix library. By systematically varying the value of K, the magnitude of the matrix coefficients can be precisely controlled. Notably, increasing K enhances the volatility of the matrix elements, which in turn provides better coefficient adjustment ability for cross-correlation optimization, supporting superior performance in the subsequent spectral reconstruction tasks. The optimal orthogonal matrix is then selected based on a target condition, with the resulting matrix weighted by the average angle sensitivity and cross-correlation coefficient. Here, the cross-correlation coefficient of the ith and jth metasurface supercells is defined as follows to measure the degree of cross-correlation:

$$\rho(T_i, T_j) = \frac{\overline{(T_i - \bar{T}_i) \times (T_j - \bar{T}_j)}}{\sigma_{T_i} \times \sigma_{T_j}}, \tag{7}$$

where T_i and T_j are the transmission spectra of the ith and jth metasurface supercells, $\bar{T}_i$ and $\bar{T}_j$ are their average values, and σ_{T_i} and σ_{T_j} are their standard deviation values, respectively. The definition of the average angle sensitivity is given by Eq. (2). In

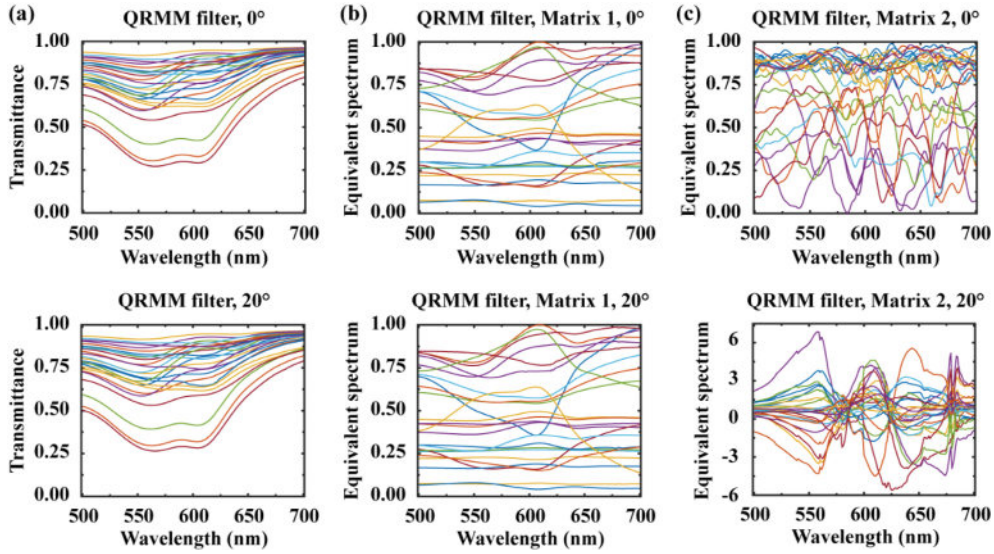

Fig. 5. (a) Transmission spectra for average polarization of the QRMM filter at the angles of 0° and 20°, respectively. Equivalent spectra for average polarization of the QRMM filter optimized by (b) Matrix 1 and (c) Matrix 2 at the angles of 0° and 20°, respectively.

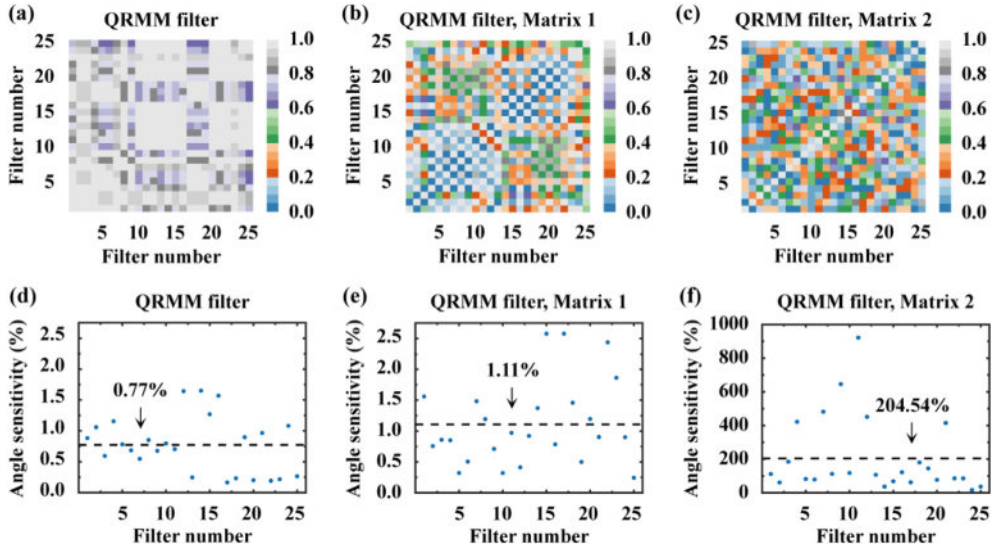

Fig. 6. (a)–(c) Cross-correlation of the QRMM filter, QRMM filter optimized by Matrix 1 and Matrix 2, respectively. (d)–(f) Angle sensitivity of the QRMM filter, QRMM filter optimized by Matrix 1 and Matrix 2, respectively. The dashed lines indicate the average angle sensitivity.

this study, we conduct an optimization procedure using two orthogonal matrices to generate diverse transmission responses at the incident angles of 0° and 20°. Matrix 1, characterized by small absolute values in Fig. 4(b), is the result of the minimal average angle sensitivity filtered by setting a cross-correlation threshold of less than 0.5. Similarly, Matrix 2, as shown in Fig. 4(c), is filtered to achieve the minimal cross-correlation and marked by its large absolute values.

B. Cross-correlation Optimization Results

Using the orthogonal Matrix 1 and Matrix 2 obtained through the aforementioned process, we optimize the QRMM filter to reduce their cross-correlation. Figure 5(a) illustrates the transmission spectra for average polarization of the original QRMM filter at the angles of 0° and 20°, respectively. Following the optimization with Matrix 1, the transmission spectra at the angles of both 0° and 20° exhibit more complex spectral features, as presented in Fig. 5(b). Concurrently, following the optimization with Matrix 2, it produces the most complex equivalent spectra in Fig. 5(c). However, this optimization also leads to significant fluctuations in angle sensitivity. Such fluctuations fall short of the criteria necessary for achieving angle-robust reconstruction.

The study further analyzes the cross-correlation coefficients and angle sensitivity of the QRMM filter before and after optimization by the orthogonal matrix. The cross-correlation coefficients and angle sensitivity of the original QRMM filter are calculated and plotted in Figs. 6(a) and 6(d). The average angle sensitivity is 0.77%, indicating high robustness of the incident angle, while the cross-correlation reaches 0.90. Following the

optimization with Matrix 1 and Matrix 2, the cross-correlation is successively reduced to 0.49 and 0.26, respectively, better aligned with the spectral reconstruction requirement, as illustrated in Figs. 6(b) and 6(c). However, the average angle sensitivity increases to 1.11% and 204.54% in Figs. 6(e) and 6(f) after these optimizations. It is demonstrated that reducing cross-correlation by modifying the orthogonal matrix comes at the cost of increased angle sensitivity. Considering the requirements of both angle sensitivity and cross-correlation, the orthogonal Matrix 1 proves to be the optimal choice and is finally selected to carry out the subsequent spectral reconstruction.

4. RESULTS

The spectral reconstruction performance of the QRMM filter is studied, and an ordinary and angle-sensitive metasurface filter is included for further comparison. The ordinary filter consists of periodic Au nanopillars arranged on a SiO_2 substrate, with a square period ranging from 240 to 480 nm. The height of the Au nanopillars is 50 nm, while their diameter ranges from 120 to 340 nm. We select a 5×5 ordinary filter with an average angle sensitivity of 11.69% and a cross-correlation of 0.71 for spectral reconstruction without any optimization applied. To assess the performance of spectral reconstruction, we use spectral fidelity as a metric, defined as follows [24]:

$$F = \left(1 - \sqrt{\frac{\sum_{i=1}^{M} \left(I_i - I_i'\right)^2}{\sum_{i=1}^{M} I_i^2}}\right), \tag{8}$$

where I and I' represent the incident spectrum and the reconstructed spectrum, respectively. This metric is more focused on spectral accuracy than the metric associated with the inner product definition in current research, effectively highlighting the distinctions at the angles of 0° and 20° in our study.

A. Computational Spectrometer Results

The study initiates the process by employing an orthogonal matrix to create an equivalent filter with reduced cross-correlation, which generates an equivalent output signal. This is followed by solving an underdetermined linear equation to reconstruct the desired signal. The spectral signal is reconstructed by the compressed sensing algorithm based on sparse optimization and dictionary learning [34–37]. Since a sparse signal is a prerequisite for compressed sensing and most natural spectra lack this property, the incident spectrum must first be processed and represented in a sparse form, described as follows [21]:

$$I = \Psi x, \tag{9}$$

where I is the incident spectrum, Ψ is the sparse matrix, and x is the sparse coefficients. Thus, Eq. (4) in this study can be rewritten as

$$S' = T'\Psi x. \tag{10}$$

Moreover, the introduction of the orthogonal matrix θ can be expressed as

$$(\theta S) = (\theta T)\,\Psi x. \tag{11}$$

In this way, the solution to the sparse coefficients can be converted to minimizing the l_2 norm:

$$\min_x || (\theta S) - (\theta T)\,\Psi x||_2^2 \quad \text{subject to } x > 0. \tag{12}$$

In practice, a smooth signal I that is an approximation of the ideal signal S can be reconstructed as a solution to a regularized objective function:

$$\min_x || (\theta S) - (\theta T)\,\Psi x||_2^2 + k||Dx||_2^2 \quad \text{subject to } x > 0, \tag{13}$$

where $k > 0$ is the weight, and Dx is the second derivative of signal x. Here, the value of k remains a constant across different angles for a filter. By achieving the optimal solution x, the incident spectrum can be calculated according to Eq. (9).

To evaluate the spectral reconstruction performance, we use the mango spectral data set for numerical simulation. The data set, acquired by Anderson *et al.*, includes hard green fruit (9711 spectra) and ripening fruit (1980 spectra) derived from 4675 mangoes across four seasons [38]. We interpolate the mango spectra to cover the wavelength range of 500–700 nm with a 1 nm interval. Then the spectral signal is reconstructed using the compressed sensing algorithm based on sparse optimization and dictionary learning. Each spectral signal takes 0.86 s for reconstruction on an AMD Ryzen 5 PRO 5650U processor.

A comparative analysis is conducted to evaluate the spectral reconstructed effect using the ordinary filter, the original QRMM filter, and the QRMM filter optimized by Matrix 1 at the angles of 0° and 20°. Here, 200 spectra from hard green fruit and 200 spectra from ripening fruit are selected for reconstruction, and the results are presented in Figs. 7(a) and 7(b). The ordinary filter exhibits average fidelities of 94.42% and 92.45% at the angle of 0°, whereas it yields average fidelities of 70.73% and 77.71% at the angle of 20°. When considering the overall average fidelity across both angles, the values are 93.44% at 0° and 74.22% at 20°, indicating poor spectral reconstruction capabilities under oblique incidence. In contrast, the QRMM filter achieves overall average fidelities of 93.10% and 89.73% at the angles of 0° and 20°, respectively. Following the optimization of Matrix 1, the overall average fidelity is enhanced to 94.40% at 0°, closely aligned with 91.64% at 20°. The instances are illustrated in Figs. 8(a) and 8(b), respectively, wherein the spectral reconstruction of hard green fruit and ripening fruit are presented. The result demonstrates that the QRMM filter with optimization offers robust and reliable spectral reconstruction capabilities across a 40° field-of-view, unlike the ordinary filter that shows a significant decline, thereby facilitating the distinction between the growth states of mangoes.

B. Hyperspectral Imaging Results

To further explore the spectral imaging capability, we employ a convolutional neural network (CNN) to reconstruct spectral images, as shown in Fig. 9(a). The upsampling operation is conducted using the compressed sensing algorithm and an orthogonal matrix, with the latter used for optimizing the equivalent signal that serves as an input for the neural network. This network comprises two convolutional layers with a dense

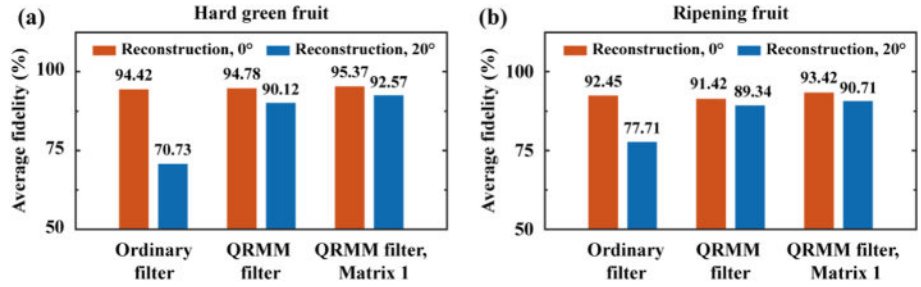

Fig. 7. Average fidelity of (a) 200 hard green fruit spectra and (b) 200 ripening fruit spectra.

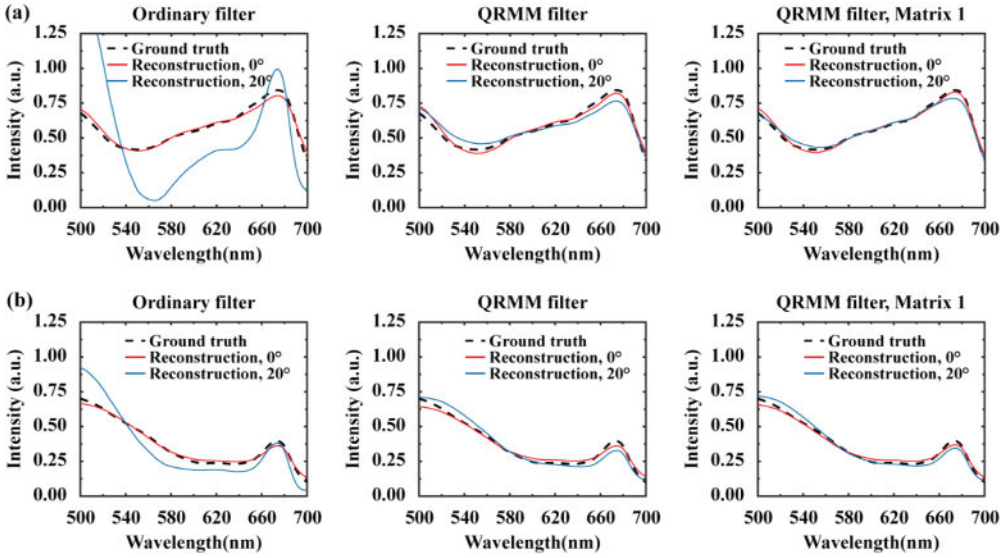

Fig. 8. Reconstructed spectra of (a) hard green fruit and (b) ripening fruit using the ordinary filter, the QRMM filter, and the QRMM filter optimized by Matrix 1 at the angles of 0° and 20°, respectively.

layer in between. The dense layer consists of dense blocks that directly connect all layers with each other, thereby enhancing feature transmission, mitigating the issue of gradient vanishing, and improving network stability [39]. The spectral image data set is acquired from the NTIRE 2022 competition [40], including images with a resolution of 482 × 512 pixels that were captured at 31 different wavelengths with a 10 nm interval. The original hyperspectral data cube is compressed in pixel dimension and interpolated in spectral dimension, resulting in a 256 × 256 × 201 data cube. Herein, the QRMM filter comprising 25 metasurface supercells is employed to reconstruct a spectrum of a single pixel, achieving a total of 201 spectral points. Subsequently, the complete hyperspectral data cube for the entire image is reconstructed through the QRMM filter arrays to collect spatial information. From the original training set, we select 900 spectral samples as the training set and validation set with a ratio of 8:2. The network is then trained for 100 epochs using the Adam optimizer with a batch size of 30. The computational performance evaluation conducted on an AMD Ryzen 5 PRO 5650U processor demonstrates a processing time of 0.49 s per image to recover the spectral data cube.

The network is then reconstructed using the ordinary filter, the original QRMM filter, and the QRMM filter optimized by Matrix 1. For visualization, the hyperspectral data cube is transformed into CIE-XYZ color space, and the reconstructed RGB images and spectra of the selected individual pixels are shown in Figs. 9(b) and 9(c). Herein, we employ the overall average fidelity to represent the mean fidelity of the results. The RGB images demonstrate excellent spectral reconstruction of the QRMM filter at the angle of 20°, with an overall average fidelity of 87.09%. This result is closely aligned with the result at 0° (overall average fidelity of 89.81%) and is significantly superior to the performance of the ordinary filter at 20° (overall average fidelity of 66.81%), which yields average fidelities of 68.85% and 64.77%. Following the optimization of Matrix 1, the overall average fidelities achieve 91.74% at 0° and 89.98% at 20°, respectively, highlighting its ability to reproduce spectral information under a 40° field-of-view. Therefore, the proposed QRMM filter optimized by Matrix 1 demonstrates high angular robustness in spectral reconstruction. Further, it can be designed to integrate with the CMOS chip for single-snapshot hyperspectral imaging.

5. CONCLUSION

In conclusion, we introduce an angle-robust hyperspectral imaging design using a 5 × 5 QRMM filter with cross-correlation optimization. The QRMM filter exhibits an average angle sensitivity of 0.77% and supports a 40° field-of-view. The orthogonal matrix-based optimization significantly reduces

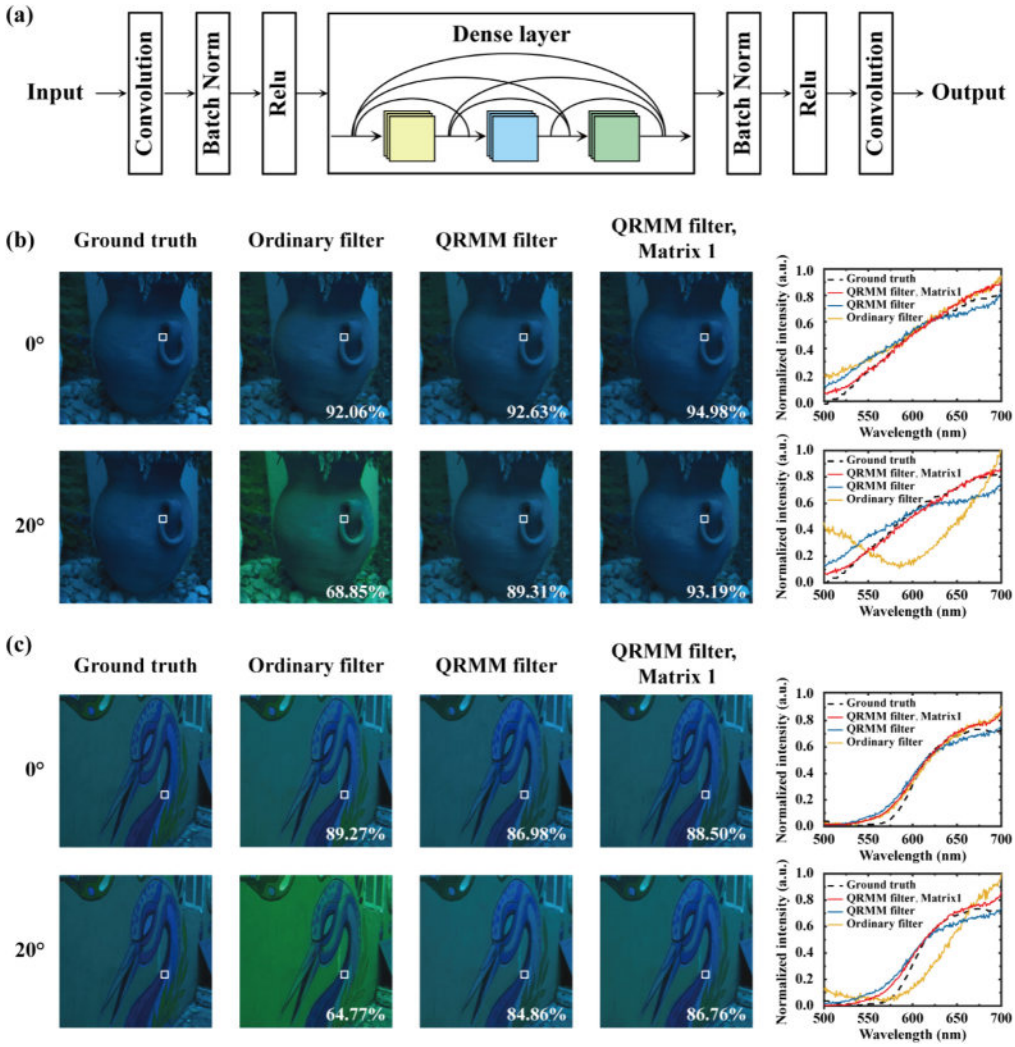

Fig. 9. (a) Architecture of convolutional neural network for spectral reconstruction. (b), (c) RGB spectral reconstruction results from NTIRE 2022, with the columns from left to right representing: ground truth, reconstructed images using the ordinary filter, the QRMM filter, the QRMM filter optimized by Matrix 1, and reconstructed spectra of the selected individual pixels indicated by the rectangular boxes at the angles of 0° and 20°.

the cross-correlation by 0.41 while maintaining a low angle sensitivity of 1.11% to align with the requirement of the compressed sensing algorithm. Spectral reconstruction results show superior angle-robust performance under oblique incidence with an average spectral fidelity of 91.64% for computational spectrometers and an average spectral image fidelity of 89.98% for hyperspectral imaging, demonstrating a balance of angle robustness and cross-correlation. This method decreases cross-correlation and effectively reduces reliance on metasurfaces, particularly for those with simple responses. Furthermore, its potential integration into portable spectral devices for single-snapshot imaging holds promise for close-up hyperspectral imaging applications, such as biological microscopic imaging, industrial defect detection, and medical endoscopic screening.

Notably, while our current investigation is limited to theoretical analysis due to experimental condition constraints, the findings provide significant guidance for experimental demonstration of angle-robust hyperspectral applications. In fact, much efforts have been made by researchers in the fabrication of metasurface structures [20,23,24], based on which we propose a feasible fabrication design incorporating appropriate dimensions and a simplified cylindrical shape to facilitate practical manufacture. The potential impact of structural fabrication errors can be effectively mitigated through precise calibration of metasurface transmission spectra. Moreover, practical spectral applications require careful consideration of several critical factors, including light source stability, module assembly alignment precision, and environmental noise interference, as these elements collectively determine system performance and measurement accuracy.

Funding. National Natural Science Foundation of China (62035016); Guandong Basic and Applied Basic Research Foundation (2023B1515040023).

Disclosures. The authors declare no conflicts of interest.

Data availability. Data underlying the results presented in this paper are not publicly available but may be obtained from the authors upon reasonable request.

REFERENCES

1. M. J. Khan, H. S. Khan, A. Yousaf, *et al.*, "Modern trends in hyperspectral image analysis: a review," IEEE Access **6**, 14118–14129 (2018).
2. M. Faraji-Dana, E. Arbabi, H. Kwon, *et al.*, "Hyperspectral imager with folded metasurface optics," ACS Photonics **6**, 2161–2167 (2019).
3. J. Luo, H. D. Zhang, S. M. Hou, *et al.*, "Confocal hyperspectral microscopic imager for the detection and classification of individual microalgae," Opt. Express **29**, 37281–37301 (2021).
4. K. Ding, M. Wang, M. Chen, *et al.*, "Snapshot spectral imaging: from spatial-spectral mapping to metasurface-based imaging," Nanophotonics **13**, 1303–1330 (2024).
5. Z. Yang, T. Albrow-Owen, H. Cui, *et al.*, "Single-nanowire spectrometers," Science **365**, 1017–1020 (2019).
6. J. Meng, J. J. Cadusch, and K. B. Crozier, "Detector-only spectrometer based on structurally colored silicon nanowires and a reconstruction algorithm," Nano Lett. **20**, 320–328 (2019).
7. J. Bao and M. G. Bawendi, "A colloidal quantum dot spectrometer," Nature **523**, 67–70 (2015).
8. Y. Zhu, X. Lei, K. X. Wang, *et al.*, "Compact CMOS spectral sensor for the visible spectrum," Photonics Res. **7**, 961–966 (2019).
9. Y. Lei, Y. Guo, M. Pu, *et al.*, "Multispectral scattering imaging based on metasurface diffuser and deep learning," Phys. Status Solidi RRL **16**, 2100469 (2022).
10. X. Hua, Y. Wang, S. Wang, *et al.*, "Ultra-compact snapshot spectral light-field imaging," Nat. Commun. **13**, 2732 (2022).
11. G. Cai, Y. Li, Y. Zhang, *et al.*, "Compact angle-resolved metasurface spectrometer," Nat. Mater. **23**, 71–78 (2024).
12. Y. Liu, Y. Shi, Y. Hu, *et al.*, "Single-pixel imaging based on metasurface fuzzy coding," Appl. Opt. **63**, 549–556 (2024).
13. N. Yu, P. Genevet, M. A. Kats, *et al.*, "Light propagation with phase discontinuities: generalized laws of reflection and refraction," Science **334**, 333–337 (2011).
14. H. T. Chen, A. J. Taylor, and N. Yu, "A review of metasurfaces: physics and applications," Rep. Prog. Phys. **79**, 076401 (2016).
15. H. Gao, X. Fan, Y. Wang, *et al.*, "Multi-foci metalens for spectra and polarization ellipticity recognition and reconstruction," Opto-Electron. Sci. **2**, 220026 (2023).
16. J. Yang, K. Cui, X. Cai, *et al.*, "Ultraspectral imaging based on metasurfaces with freeform shaped meta-atoms," Laser Photonics Rev. **16**, 2100663 (2022).
17. Z. Wu, Z. Zhang, Y. Xu, *et al.*, "Random color filters based on an all-dielectric metasurface for compact hyperspectral imaging," Opt. Lett. **47**, 4548–4551 (2022).
18. Y. Lei, Q. Zhang, Y. Guo, *et al.*, "Snapshot multi-dimensional computational imaging through a liquid crystal diffuser," Photonics Res. **11**, B111–B124 (2023).
19. Q. Zhang, Z. Yu, X. Liu, *et al.*, "End-to-end joint optimization of metasurface and image processing for compact snapshot hyperspectral imaging," Opt. Commun. **530**, 129154 (2023).
20. H. He, Y. Zhang, Y. Shao, *et al.*, "Meta-attention network based spectral reconstruction with snapshot near-infrared metasurface," Adv. Mater. **36**, 2313357 (2024).
21. Z. Wang, S. Yi, A. Chen, *et al.*, "Single-shot on-chip spectral sensors based on photonic crystal slabs," Nat. Commun. **10**, 1020 (2019).
22. W. Zhang, H. Song, X. He, *et al.*, "Deeply learned broadband encoding stochastic hyperspectral imaging," Light Sci. Appl. **10**, 108 (2021).
23. J. Yang, K. Cui, Y. Huang, *et al.*, "Angle-insensitive spectral imaging based on topology-optimized plasmonic metasurfaces," Laser Photonics Rev. **18**, 2400255 (2024).
24. C. Chen, X. Li, G. Yang, *et al.*, "Computational hyperspectral devices based on quasi-random metasurface supercells," Nanoscale **15**, 8854–8862 (2023).
25. K. Guo, D. Yang, B. Liu, *et al.*, "Random broadband filters based on combination of metasurface and multilayer thin films for hyperspectral imaging," J. Phys. D. **57**, 315103 (2024).
26. P. B. Johnson and R. W. Christy, "Optical constants of the noble metals," Phys. Rev. B **6**, 4370–4379 (1972).
27. E. D. Palik, *Handbook of Optical Constants of Solids* (Academic, 1998).
28. V. G. Kravets, A. V. Kabashin, W. L. Barnes, *et al.*, "Plasmonic surface lattice resonances: a review of properties and applications," Chem. Rev. **118**, 5912–5951 (2018).
29. J. Cao, T. Sun, and K. T. Grattan, "Gold nanorod-based localized surface plasmon resonance biosensors: a review," Sens. Actuators B Chem. **195**, 332–351 (2014).
30. C. Yang, W. Shen, J. Zhou, *et al.*, "Angle robust reflection/transmission plasmonic filters using ultrathin metal patch array," Adv. Opt. Mater. **4**, 1981–1986. (2016).
31. C. L. Tan, S. J. Jang, and Y. T. Lee, "Localized surface plasmon resonance with broadband ultralow reflectivity from metal nanoparticles on glass and silicon subwavelength structures," Opt. Express **20**, 17448–17455 (2012).
32. E. J. Candès, "Compressive sampling," in *Proceedings of the International Congress of Mathematicians* (International Mathematical Union, 2006), Vol. **3**, pp. 1433–1452.
33. D. L. Donoho, "Compressed sensing," IEEE T. Inform. Theory **52**, 1289–1306 (2006).
34. X. Yuan, D. J. Brady, and A. K. Katsaggelos, "Snapshot compressive imaging: theory, algorithms, and applications," IEEE Signal Process. Mag. **38** (2), 65–88 (2021).
35. M. Aharon, M. Elad, and A. Bruckstein, "K-SVD: an algorithm for designing overcomplete dictionaries for sparse representation," IEEE Trans. Signal Process. **54**, 4311–4322 (2006).
36. M. Grant and S. Boyd, CVX: Matlab software for disciplined convex programming, version 2.2, 2014, http://cvxr.com/cvx.
37. M. Grant and S. Boyd, "Graph implementations for nonsmooth convex programs," in *Recent Advances in Learning and Control*, V. Blondel, S. Boyd, H. Kimura, *et al.*, eds. Lecture Notes in Control Inf. Sci. (Springer-Verlag Limited, 2008), pp. 95–110.
38. N. T. Anderson, K. B. Walsh, P. P. Subedi, *et al.*, "Achieving robustness across season, location and cultivar for a NIRS model for intact mango fruit dry matter content," Postharvest Biol. Technol. **168**, 111202 (2020).
39. G. Huang, Z. Liu, L. v. d. Maaten, *et al.*, "Densely connected convolutional networks," in *Proceedings of IEEE Conference on Computer Vision and Pattern Recognition* (2017), pp. 2261–2269.
40. B. Arad, R. Timofte, R. Yahel, *et al.*, "NTIRE 2022 spectral recovery challenge and data set," in *IEEE/CVF Conf. Comput. Vision Pattern Recogn.* (2022), 863–881.